Chemical Science

ROYAL SOCIETY OF CHEMISTRY

EDGE ARTICLE

View Article Online
View Journal

Cite this: DOI: 10.1039/d5sc08632a

All publication charges for this article have been paid for by the Royal Society of Chemistry

Beyond the Lindlar catalyst: highly-oxidized Pd single atoms as promoters for alkyne semi-hydrogenation

Ming Jiang,†[a] Yao Lv,†[b] Zhongzhe Wei,*[a] Xu Liu,[a] Zhixiang Yang,[a] Chuanming Chen,[a] Yiming Hu,[a] Fangjun Shao,[a] Xiaonian Li,[a] Jiaxing Hu,*[c] Sheng Dai *[b] and Jianguo Wang *[a]

The semi-hydrogenation of alkynes is crucial for the synthesis of steroid hormone drugs, yet conventional approaches relying on Pd surface poisoning additives sacrifice activity and sustainability for selectivity. Herein, we present a "grafting-then-coordination" strategy to construct a Pd/C–NH_2 catalyst featuring coexisting tetravalent Pd single atoms (Pd_{IV} SAs) and Pd nanoparticles (NPs), which achieves inhibitor-free and highly efficient hydrogenation of steroidal alkynes. The Pd/C–NH_2 catalyst, functionalized with 3-aminopropyltriethoxysilane (APTES), exhibits 99% conversion with 97% selectivity in the selective hydrogenation of mifepristone under 0.1 MPa at 25 °C, with a remarkable turnover frequency (TOF) of 3675 h^{-1}, representing a 17-fold enhancement over the conventional Lindlar catalyst. Mechanistic studies reveal that the Pd_{IV} SAs are stabilized through Pd–N/O coordination by leveraging oxygen-containing groups of the support and amino groups of the ligand. The electron-deficient Pd_{IV} SAs adsorb mifepristone, mitigating substrate self-poisoning on Pd NPs, while Pd NPs activate H_2 and promote hydrogen spillover to Pd_{IV} SAs, enabling hydrogenation *via* a dual-site cooperative mechanism. The stable Pd_{IV} SAs transform conventional poisoning sites into productive active centers, offering valuable insights for the rational design of advanced selective hydrogenation catalysts.

Received 6th November 2025
Accepted 5th January 2026

DOI: 10.1039/d5sc08632a

rsc.li/chemical-science

Introduction

The semi-hydrogenation of alkynes is crucial for the synthesis of fine chemicals, pharmaceuticals, and petrochemicals[1–3] and is particularly indispensable in the production of steroid hormone drugs.[4] In 2016, global sales of steroid hormone medications surpassed $100 billion, making them the second-largest class of drugs after antibiotics,[5] reflecting their critical role in regulating biological functions. Aglepristone, the semi-hydrogenated derivative of mifepristone, acts as a progesterone antagonist[6] and is widely employed in the treatment of insulin-resistant diabetes and acromegaly. Product selectivity directly influences the final purity, yield, and economic feasibility of the manufacturing process.[7,8] Compared to simpler alkynes such as phenylacetylene, steroidal alkynes possess a polycyclic structure that leads to stronger adsorption on catalyst surfaces, exacerbating the competitive adsorption–desorption dynamics between alkynes and alkenes.[9–11] Furthermore, the steric bulk of mifepristone-derived molecules introduces mass transfer constraints that hinder access to active sites.[12–14] Consequently, the hydrogenation process faces dual challenges of low selectivity and insufficient activity. Thus, the development of efficient catalysts for the semi-hydrogenation of steroidal alkynes, along with a deeper understanding of how the catalysts modulate adsorption and desorption behavior, remains a central goal in this field.

Pd-based catalysts are widely used in alkyne semi-hydrogenation due to their excellent ability in H_2 activation. However, the strong adsorption of alkynes on continuous Pd surfaces often leads to over-hydrogenation.[11,15,16] In industrial catalysis, the Lindlar catalyst[17–19] is regarded as a benchmark for alkyne semi-hydrogenation. Although it offers good selectivity, its Pb-containing components pose environmental risks and significantly reduce both catalytic activity and metal utilization, limiting its industrial applicability. Alternatively, strategies such as alloying to modify electronic properties,[15,20–22] doping with inexpensive metals,[23–25] or partial poisoning of active centers[26–29] have been employed to disrupt the Pd ensemble effect and thereby promote alkene desorption. Unfortunately, these

[a]State Key Laboratory of Green Chemical Synthesis and Conversion, Zhejiang Key Laboratory of Surface and Interface Science and Engineering for Catalysts, College of Chemical Engineering, Zhejiang University of Technology, Hangzhou 310032, China. E-mail: weizhzhe@zjut.edu.cn; jgw@zjut.edu.cn

[b]Key Laboratory for Advanced Materials and Feringa Nobel Prize Scientist Joint Research Center, School of Chemistry and Molecular Engineering, East China University of Science & Technology, Shanghai 200237, P. R. China. E-mail: shengdai@ecust.edu.cn

[c]Zhejiang Huahai Pharmaceutical Co. Ltd, Linhai 317024, P. R. China. E-mail: hujiaxing@huahaipharm.com

† Both authors contributed equally to this work.

approaches usually result in reduced activity and lower metal utilization[30,31] Recent studies show that single-atom (SA) catalysts are highly effective in promoting alkene desorption.[32–34] Their isolated sites not only eliminate the geometric effects associated with multi-site adsorption[35] but also feature electron-deficient metal centers[36] that reduce electronic back-donation to olefin products. This weakens the adsorption strength of alkenes and facilitates their desorption, thereby enhancing selectivity towards alkenes. Studies have shown that the valence state of Pd SAs can be tuned between 0 and +2;[33,34,37,38] however, the specific catalytic mechanism of more electron-deficient states (such as Pd^{4+}) in hydrogenation reactions remains unclear. More critically, unstable high-valent Pd^{4+} species have only been observed in certain complexation scenarios, typically with the combination of potential oxidants[39,40] such as mer-tridentate carbene pincers and chelating bipyridyl. Furthermore, under reductive reaction atmospheres, Pd^{4+} is prone to reduction or aggregation, leading to structural degradation.[40] Therefore, the controllable synthesis and long-term stability of Pd_{IV} SAs still face significant challenges. Moreover, Pd SAs with isolated sites exhibit poor H_2 dissociation capability[41,42] and often require harsh reaction conditions to achieve efficient hydrogenation. In the hydrogenation of mifepristone, its polycyclic structure tends to strongly adsorb on Pd surfaces, blocking active sites and making efficient H_2 activation particularly crucial. Constructing a catalytic system with coexisting single atoms and nanoparticles may synergistically enhance both activity and selectivity, offering a promising path to overcome current limitations.

This work presents a ligand modification strategy for the controlled construction of a synergistic catalytic system with coexisting Pd_{IV} SAs and Pd NPs, achieving highly efficient and selective hydrogenation of mifepristone. Leveraging the abundant surface hydroxyl (–OH) and carbonyl (C=O) groups on the carbon support, a precise "grafting-then-coordination" mechanism is established: under aqueous conditions, surface hydroxyl groups facilitate the hydrolysis and condensation of 3-aminopropyltriethoxysilane (APTES), forming covalent Si–O–C bonds that graft amino groups ($-NH_2$) onto the carrier. Subsequently, C=O and $-NH_2$ groups act as coordination sites to stabilize Pd species, forming structurally stable Pd_{IV} SAs. This approach allows quantitative tuning of the active site ratio, thereby optimizing the synergistic interplay between Pd_{IV} SAs and Pd NPs. Under mild conditions (25 °C, 0.1 MPa), the optimized Pd/C–NH_2 catalyst exhibits exceptional performance in the semi-hydrogenation of mifepristone, achieving 99% conversion, 97% selectivity, and a TOF of 3675 h^{-1}, significantly outperforming the performance of commercial Pd/C and the Lindlar catalyst. Mechanistic investigations reveal that Pd_{IV} SAs adsorb mifepristone, mitigating substrate self-poisoning on Pd NPs, while Pd NPs activate H_2 and promote hydrogen spillover to hydrogen-deficient Pd_{IV} SAs, collectively enabling hydrogenation *via* a dual-site cooperative mechanism. The ligand modification strategy not only stabilizes metastable Pd_{IV} SAs but also alleviates competitive adsorption between H_2 and mifepristone, ultimately enabling highly efficient and selective hydrogenation.

Experimental

Synthesis of C–NH_2-*t*

500 mg of activated carbon was dispersed in 50 mL of deionized water and subjected to ultrasonication for 30 min. Then, 3-aminopropyltriethoxysilane (APTES) was added, and the mixture was stirred at 35 °C for 12 h, with a mass ratio of carrier to modifier fixed at 1 : 2. The resulting product was filtered under vacuum, thoroughly washed with deionized water until the filtrate reached neutral pH and dried overnight at 70 °C to obtain C–NH_2. Using the same conditions and an equivalent amount of modifier, a series of APTES-modified carriers designated as C–NH_2-*t* (where *t* denotes the stirring time with the modifier: t = 5, 12, and 24 h) were prepared under different modification durations. Furthermore, the mass ratio between activated carbon and APTES, as well as the type of silane coupling agent, was systematically screened.

Synthesis of Pd/C–NH_2-*t*

A series of Pd-based catalysts were prepared using the impregnation method. Specifically, 500 mg of C–NH_2-*t* support was dispersed in 30 mL of deionized water and ultrasonicated for 30 min. An aqueous solution of K_2PdCl_4 (containing 20 mg per mL Pd) was added, and the mixture was stirred at 35 °C for 1 h. Then, 10 mL of a freshly prepared sodium borohydride solution (20 mg mL^{-1}) was added, with stirring continued for 1 h. The resulting solid was collected by vacuum filtration, washed thoroughly, and dried at 70 °C for 12 h to obtain Pd/C–NH_2-*t*. For comparison, a reference catalyst Pd/C was synthesized using the same procedure with unmodified activated carbon as the support. Additional control catalysts were also prepared *via* the same impregnation approach using supports synthesized under different conditions. The theoretical Pd loading in all catalysts was 5 wt%.

Results and discussion

Fabrication and characterization of catalysts

The simultaneous and controlled distribution of Pd_{IV} SA and Pd NP active centers on activated carbon was achieved through a stepwise process involving initial grafting of functional ligands onto the support, followed by precise metal coordination and reduction, as illustrated in Fig. 1a. The carbon support rich in oxygen-containing functional groups was first modified with APTES. The surface hydroxyl groups on the carbon guide the hydrolysis of APTES, leading to the elimination of an ethanol molecule and formation of covalent Si–O–C bonds, thereby grafting $-NH_2$ groups onto the carbon framework.[43] The introduction of $-NH_2$ plays a crucial role in controlling the dispersion of metal nanostructures,[44] which is beneficial for the formation of uniformly distributed and smaller-sized Pd species. Subsequent wet impregnation with an aqueous K_2PdCl_4 solution and reduction with $NaBH_4$ yielded a series of catalysts labeled as Pd/C–NH_2-*t* (where *t* represents the APTES modification time). The optimal catalyst, Pd/C–NH_2, was obtained after 12 h of APTES modification.

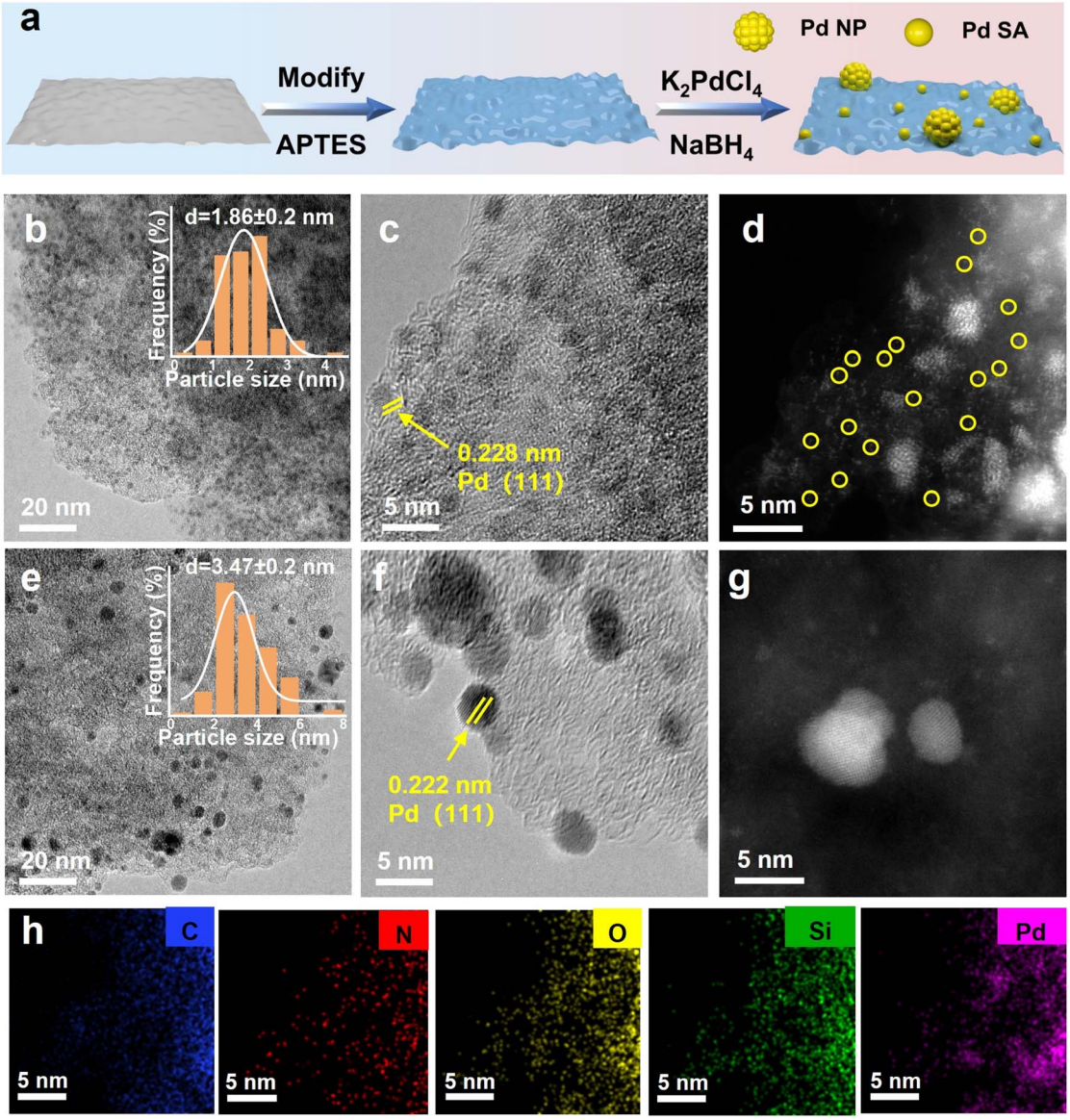

Fig. 1 Characterization of Pd/C–NH_2 and Pd/C. (a) Schematic illustration for the synthetic processes of Pd/C–NH_2. (b, c, e and f) TEM and HRTEM images of Pd/C–NH_2 and Pd/C. (d and g) AC-STEM images of Pd/C–NH_2 and Pd/C. (h) EDS elemental distribution diagram of Pd/C–NH_2.

Inductively coupled plasma optical emission spectrometry (ICP-OES) analysis confirmed Pd loadings of 4.95% for Pd/C and 4.93% for Pd/C–NH_2 (Table S1), indicating no substantial metal loss during functionalization. High-resolution transmission electron microscopy (HRTEM) and high-angle annular dark-field scanning transmission electron microscopy (HAADF-STEM) images, combined with aberration-corrected transmission electron microscopy (AC-STEM) results (Fig. 1b–g, and S1–6), revealed a broad size distribution of Pd NPs in the unmodified Pd/C catalyst, with an average size of 3.47 nm. The observed lattice spacing of 0.222 nm corresponds to the Pd (111) plane. In contrast, the APTES-modified Pd/C–NH_2-*t* catalyst exhibits a higher density of finely dispersed and narrowly distributed Pd NPs, along with evidence of Pd SAs. Notably, Pd/C–NH_2 shows Pd NPs averaging only 1.86 nm in size, with an observed interplanar spacing of 0.228 nm corresponding to the Pd (111) surface. These results indicate that the –NH_2 ligand modification significantly enhances the dispersion of Pd. Electron microscopy observations with aberration corrected transmission electron microscopy (Fig. 1d and g) demonstrate that the APTES-modified catalyst not only carries smaller Pd NPs but also contains abundant Pd SAs. Energy-dispersive X-ray (EDX) analysis in Fig. 1h reveals a homogeneous distribution of C, N, O, Si and Pd elements throughout the catalyst. The intensified nitrogen signal confirms the successful incorporation of –NH_2 groups into the support. Hydrogen–oxygen titration measurements (H_2–O_2) indicated a remarkable increase in Pd dispersion from 15.55% to 43.31% after APTES modification (Table S2), unequivocally demonstrating that APTES functionalization substantially improves the dispersion of Pd species on the carbon support. To determine the valence states of the Pd atoms, spherical aberration-corrected transmission electron

microscopy combined with electron energy loss spectroscopy (EELS) was employed to characterize the Pd/C–NH_2 composite (Fig. S7). As EELS analysis at the single-atom level was not feasible, the investigation focused specifically on Pd NPs. The observed high-energy shift in the EELS spectra indicated the presence of Pd atoms in higher oxidation states.[45] Three distinct Pd NP models exhibited EELS profiles with energy positions situated between those of the Pd^0 and Pd^{2+} reference standards, suggesting that the bonded Pd atoms in Pd NPs are in an oxidation state of $Pd^{\delta+}$ ($0 < \delta < +2$).

X-ray diffraction (XRD) patterns (Fig. 2a, and S8) of Pd/C and Pd/C–NH_2 exhibit a characteristic peak at near $2\theta = 23°$, corresponding to the (002) plane of the carbon material, indicating a high degree of graphitization.[46] The distinctive peaks observed at $2\theta = 40°$, 46°, and 68° for Pd/C are assigned to the (111), (200), and (220) planes of metallic Pd,[47] respectively. As the time for APTES modification increased, the intensity of the Pd peaks gradually diminished and eventually disappeared, indicating a reduction in particle size. This phenomenon is consistent with the results of electron microscopy. Raman spectroscopy (Fig. S9 and Table S3) further analyzed the carbon structure of the two catalysts. Signals at 1345–1351 cm^{-1} and 1597–1603 cm^{-1} correspond to the D-band (defect-related) and G-band (graphitization-related), respectively. The nearly identical I_D/I_G ratio of Pd/C–NH_2 (2.27) and Pd/C (2.25) indicated that the APTES modification did not affect the graphitization level of the carbon framework.[48] Fourier transform infrared spectroscopy (FT-IR) confirmed the successful grafting of APTE, as evidenced by a new absorption band at 1597 cm^{-1} in Pd/C–NH_2-*t*, attributed to the –N–H stretching vibration of the amino-silane (Fig. 2b and S10).[43] N_2 adsorption–desorption isotherms shown in Fig. S11 and Table S4 revealed a reduction in specific surface area and pore volume after APTES modification, but an increased mean pore size (from 3.8 to 6.9 nm), which can promote the diffusion of mifepristone considering its large steric hindrance. After Pd loading, the catalysts showed similar specific surface areas and pore sizes with the support, preserving a mesoporous structure. X-ray photoelectron spectroscopy (XPS) was employed to explore the surface composition and electronic interactions between components of catalysts (Fig. 2c–e, and S12–16). The appearance of N 1s and Si 2p signals after modification further confirmed the successful introduction of APTES. High-resolution O 1s spectra distinguishes 529.6 eV for lattice oxygen (O_{latt}) from 532.1 eV for

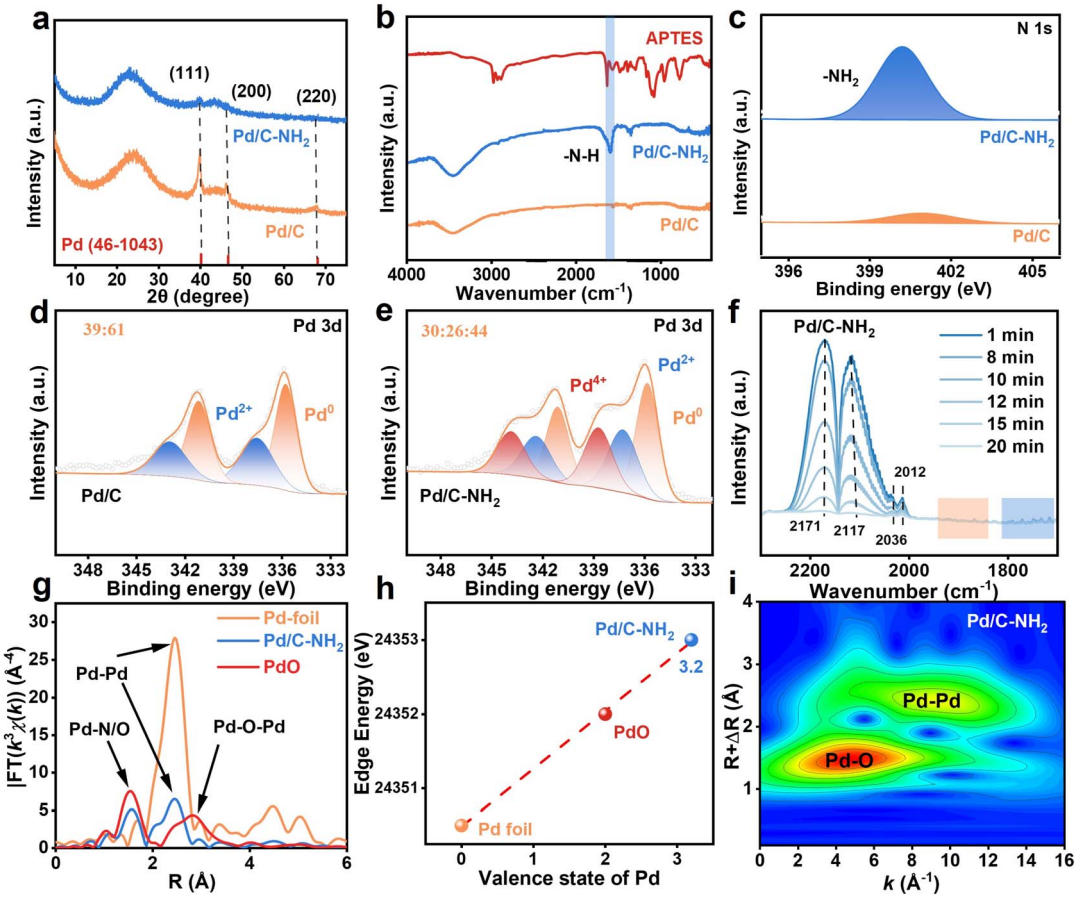

Fig. 2 Structure characterization of Pd/C–NH_2. (a) XRD patterns of Pd/C and Pd/C–NH_2. (b) FTIR spectra of APTES, Pd/C and Pd/C–NH_2. (c–e) High-resolution N 1s and Pd 3d XPS spectra of Pd/C and Pd/C–NH_2. (f) CO-DRIFTS spectra of Pd/C–NH_2. (g) FT-EXAFS spectra of Pd/C–NH_2, Pd foil, and PdO. (h) The average oxidation states of Pd species in the catalysts determined by Pd K-edge XANES analysis. (i) Wavelet-transformed spectra of Pd/C–NH_2.

adsorbed oxygen (O_{ads}).[28] The high-resolution C 1s spectrum exhibits distinct peaks at 286.3 eV and 288.2 eV, corresponding to –C–O and C=O bonds, respectively. The abundance of oxygen-containing functional groups in Pd/C–NH_2 facilitates APTES grafting and subsequently coordination with Pd to form Pd_{IV} SAs. High-resolution Pd 3d spectra confirmed the coexistence of Pd^0 and Pd^{2+} species in Pd/C, with characteristic binding energies observed at 335.3 eV (Pd^0 $3d_{5/2}$), 340.6 eV (Pd^0 $3d_{3/2}$), 336.5 eV (Pd^{2+} $3d_{5/2}$), and 342.8 eV (Pd^{2+} $3d_{3/2}$). Notably, two additional peaks appeared at 338.3 eV and 344.5 eV in Pd/C–NH_2, exhibiting intensities even higher than those of the Pd^{2+} species. These peaks can be assigned to the $3d_{5/2}$ and $3d_{3/2}$ orbitals of Pd^{4+}, respectively.[49,50] In the unmodified Pd/C catalyst, Pd^0 constitutes 61% of the Pd species, whereas in Pd/C–NH_2, the proportion of Pd^0 decreases to 44%, with Pd^{4+} accounting for 30%. The presence of Pd^{2+} is commonly attributed to the surface oxidation during synthesis. Interestingly, the APTES-modified catalyst exhibited an even higher oxidation state of Pd^{4+} than Pd^{2+}, and the proportion of Pd^{4+} increased as the APTES modification time extended. EELS analysis showed that Pd NPs primarily exhibit oxidation states between 0 and +2, suggesting that the observed Pd^{4+} species in Pd/C–NH_2 originate from atomically dispersed Pd, indicative of the successful formation of Pd_{IV} SAs after modification. Unexpectedly, XPS analysis of the catalyst Pd/C–NH_2-unreduced (synthesized identically but without $NaBH_4$ reduction) also revealed that it contained 34% Pd^{4+} (Fig. S17). This suggests that Pd^{4+} species form during the loading step and remain stable even under the strong reducing conditions of $NaBH_4$ treatment. The local environment of palladium species on the support was further characterized by CO-DRIFT spectroscopy (Fig. 2f, and S18). The characteristic peaks observed at 2170 cm^{-1} and 2117 cm^{-1} correspond to free CO molecules. Notably, the peaks at 2036 cm^{-1} and 2012 cm^{-1} for Pd/C–NH_2 showed significantly higher intensity than those for Pd/C. The peak at 2036 cm^{-1} can be assigned to the symmetric stretching vibration of gem-dicarbonyl doublet CO on positively charged Pd species, while the peak at 2012 cm^{-1} corresponds to the stretching vibrations of linearly adsorbed CO on isolated Pd sites and bridge-adsorbed CO on ultrasmall Pd clusters. Additionally, the characteristic peaks in the 1840–1940 cm^{-1} range indicate the presence of bridge-adsorbed CO on Pd nanoparticles, while those in the 1700–1820 cm^{-1} range are attributed to triply coordinated adsorbed CO. These spectral features confirm that the modification treatment successfully constructed isolated Pd SAs in addition to the original Pd NPs. These spectroscopic assignments align well with AC-STEM imaging data.[51,52]

To gain deeper insight into the local coordination environment of Pd, X-ray absorption fine structure (XAFS) measurements were conducted at the Pd K-edge.[49,50] As shown in Fig. 2g, Fourier transform (FT) K^2-weighted EXAFS analysis of Pd/C–NH_2 shows a pronounced coordination peak at approximately 2.74 Å in *R*-space, corresponding to Pd–Pd scattering paths. This peak is markedly weaker than that of the electron transfer. The *k*-space EXAFS spectra and their corresponding fits for Pd/C–NH_2 and reference samples display similar oscillatory behavior in the low-*k* region (3–9 $Å^{-1}$). The high accuracy of the fitting was validated by an *R*-factor of 0.0075, significantly lower than the reference threshold of 0.024748. Wavelet transform (WT) EXAFS analysis (Fig. 2i) further discriminates these bonding types. The wavelet contour plot of Pd/C–NH_2 exhibits maximum intensity at 2.0–3.0 Å and 9.0 $Å^{-1}$, indicative of Pd–Pd coordination, alongside a new feature at 1.0–2.0 Å and 4.2 $Å^{-1}$, corresponding to Pd–N/O coordination. This confirms that Pd species are coordinated not only to each other but also to N/O atoms from the support. Quantitative EXAFS fitting (Fig. S19 and Table S5) provided coordination numbers of 3.1 ± 0.2 for Pd–N/O and 3.0 ± 0.1 for Pd–Pd, with bond lengths of 2.028 ± 0.005 Å and 2.739 ± 0.004 Å, respectively. XAFS data and fitting results demonstrates that Pd/C–NH_2 contains both Pd–N/O and Pd–Pd coordination environments, indicating the presence of both Pd SAs and small-sized Pd NPs in Pd/C–NH_2. Furthermore, by establishing a linear relationship between absorption edge energy and known valence states of Pd foil and PdO, the average oxidation state of Pd in Pd/C–NH_2 was effectively semi-quantitatively determined to be +3.2 (Fig. 2h). Given that EELS analysis indicated that the valence state of Pd NPs is between 0 and +2, an average oxidation state of +3.2 significantly exceeds the expected range for metallic Pd or PdO nanoparticle-based configurations. This suggests the presence of Pd species with a valence state higher than +3.2 in the system. Combined with the observation of 30% Pd^{4+} content in XPS characterization, it further confirms that the Pd SAs in the catalyst are in the +4 oxidation state. Therefore, ligand modification enables the synthesis of a catalyst containing stable Pd_{IV} SAs, as unequivocally confirmed by complementary XAFS, XPS, and EELS analyses.

Study on the formation mechanism of Pd_{IV} SAs

Pd^{4+} is notoriously difficult to form under conventional conditions, and it typically exists as a highly unstable intermediate[39,40,53] when it does occur. Remarkably, in our system, we have successfully synthesized stable Pd_{IV} SAs, making it essential to elucidate their formation mechanism. Preliminary experiments indicated that the introduction of APTES is crucial for the formation of Pd_{IV} SAs. APTES, a silane coupling agent, contains both an –NH_2 terminal and a hydrolyzable –Si–O terminal.[43] To clarify the role of these functional groups, we modified the support using *n*-butylamine (which possesses only an –NH_2 group) to prepare the Pd/C–NBA catalyst. XPS characterization revealed that although Pd_{IV} formed in Pd/C–NBA, the proportion of Pd^{4+} was 19%, significantly lower than that in Pd/C–NH_2. Nevertheless, this confirms that Pd^{4+} can still form under these conditions. Subsequently, we used *n*-propyltriethoxysilane, which lacks an –NH_2 group, to synthesize the Pd/C–CH_3 catalyst. Interestingly, no Pd^{4+} was detected in Pd/C–CH_3, indicating that the –NH_2 group is indeed indispensable for the formation of Pd^{4+} (Fig. 3a, S20 and 21). Furthermore, the effect of the –NH_2 group is closely related to the hydrolysis degree of the silane grafted on the carbon support. Therefore, we proposed to control the content of Pd_{IV} SAs by regulating the hydrolysis degree of the silane coupling agent. This was approached from two perspectives: first, the oxygen-containing functional groups on the carbon surface were

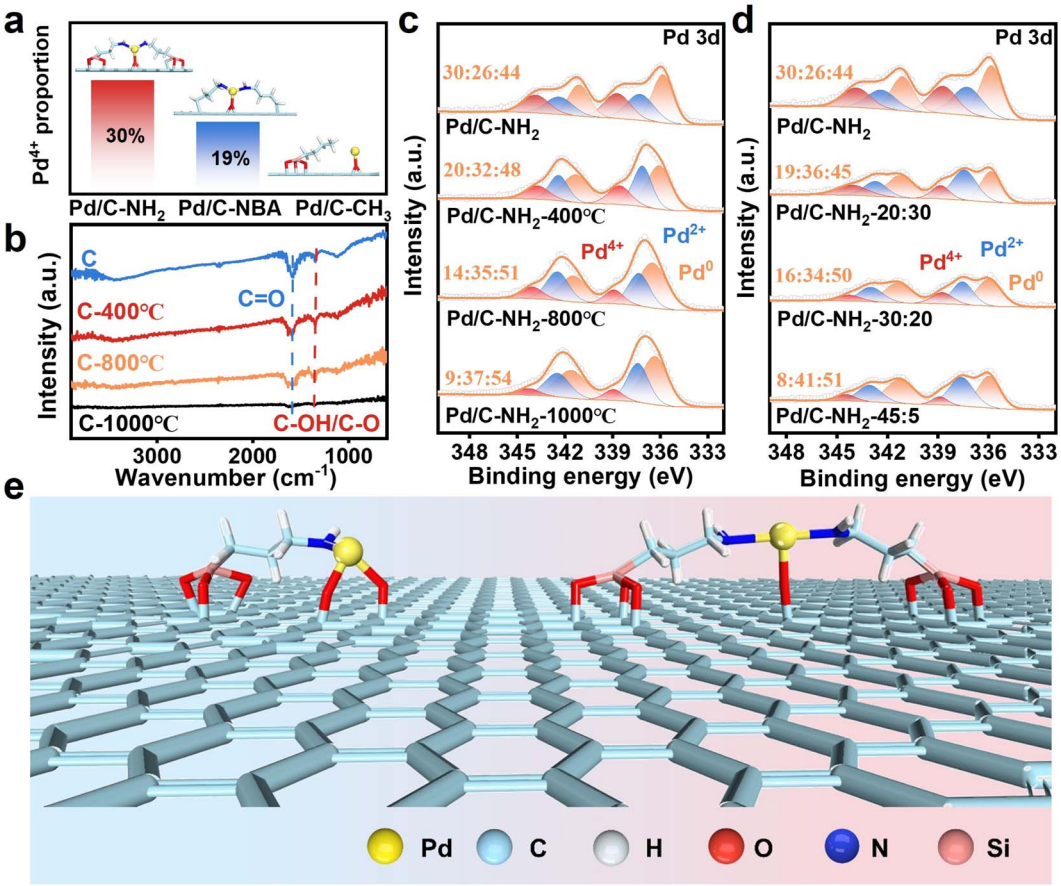

Fig. 3 Formation mechanism of Pd^{4+} in Pd/C–NH_2. (a) The proportion of Pd^{4+} in catalysts modified with different silane coupling agents. (b) FT-IR spectra of catalysts with supports calculated at different temperatures. (c) High-resolution Pd 3d XPS spectra of catalysts with supports calculated at different temperatures. (d) High-resolution Pd 3d XPS spectra of catalysts with different $V_{EtOH}:V_{H_2O}$ ratios for hydrolysis. (e) Schematic diagram of the grafting form of the ligand, support and Pd in Pd/C–NH_2.

reduced by high-temperature calcination under an inert atmosphere. We observed that the Pd^{4+} content decreased significantly with increasing calcination temperature (Fig. 3c). In the FT-IR spectra (Fig. 3b), the characteristic peaks at 1345 cm^{-1} and 1590 cm^{-1} are attributed to the stretching vibrations of C–OH/C–O and C=O bonds,[54] respectively. The intensity of these peaks gradually weakened with increasing calcination temperature and almost vanished at 1000 °C, indicating extensive removal of oxygen-containing functional groups. After the carbon was calcined at 1000 °C and treated with APTES under identical modification conditions, only 9% of Pd^{4+} was detected in Pd/C–NH_2-1000 °C, demonstrating that oxygen-containing functional groups on the support surface are critical for APTES hydrolysis. That is, the carbon support possesses sufficient –OH and C=O groups to facilitate both APTES hydrolysis/grafting and subsequent Pd–N/O coordination. Additionally, the hydrolysis rate was adjusted by varying the ratio of ethanol to water during hydrolysis. As expected, the introduction of ethanol may inhibit the hydrolysis of APTES.[55] When the modification was carried out with an ethanol-to-water volume ratio of 45 : 5, only 8% of Pd^{4+} species were formed (Fig. 3d). This indicates that the hydrolysis–condensation reaction of APTES proceeds most rapidly under pure aqueous conditions, resulting in the highest grafting density of –NH_2 groups on the carbon support and consequently leading to the highest content of Pd^{4+}.

Based on the above findings, we conclude that the formation and stabilization of Pd_{IV} SAs arise from the synergistic interplay between oxygen-containing functional groups on the support surface and the –NH_2 groups from the ligand. EXAFS fitting revealed a Pd–N/O coordination number of 3.1, indicating that Pd_{IV} SAs are stabilized through coordination with both N from the ligand and O from the carrier.[29] We therefore propose that Pd_{IV} SAs are coordinated in either a [Pd–N_1O_2] or [Pd–N_2O_1] configuration (Fig. 3e). The "grafting-then-coordination" regulation mechanism enables precise Pd–N/O coordination. Under aqueous conditions, the –OH groups on the carrier surface promote the hydrolysis and condensation of APTES, forming covalent Si–O–C bonds and thereby grafting –NH_2 onto the carbon support. Subsequently, C=O and –NH_2 groups act as coordination sites to anchor Pd species into a well-defined geometry, leading to the formation of stable Pd_{IV} SAs. By controlling the concentration of oxygen species on the support as well as the hydrolysis rate of the silane ligand, the proportion of SA active sites can be quantitatively

tailored, enabling precise regulation of the synergistic catalysis between Pd_{IV} SAs and Pd NPs.

Catalytic performance

This study evaluated the performance of the synthesized catalysts in the semi-hydrogenation of mifepristone. To eliminate the influence of mass transfer on the reaction rate, the semi-hydrogenation of mifepristone was conducted under varying catalyst mass (internal diffusion) and stirring speed (external diffusion). As shown in Fig. S22 and S23, the conversion of mifepristone showed a linear correlation with catalyst mass. When the stirring speed exceeded 800 rpm, the conversion rate remains essentially unchanged, indicating that mass transfer limitations are negligible under the current reaction conditions. As illustrated in Fig. 4a, a comparison among different silane coupling agents revealed that APTES exhibited superior activity and selectivity under the same treatment conditions. By optimizing the ligand content and modification time (Fig. S24 and S25), it was found that the optimal mass ratio of carbon to APTES was 1 : 2, beyond which further increases in ligand content had minimal impact on catalytic performance. Catalytic activity increased with longer modification time, while the selectivity remained consistently above 93%, which further verifies the promoting effect of APTES modification on the catalytic performance. Consequently, the optimal catalyst preparation conditions were determined as follows: $m_C : m_{APTES} = 1 : 2$, with APTES modification conducted at 35 °C for 12 h. Next, we focused on comparing the catalytic performance of the Pd/C and Pd/C–NH_2 catalysts. As shown in Fig. 4b, c and S26, under identical reaction conditions (25 °C, 0.1 MPa), the Pd/C–NH_2 catalyst achieved 99% conversion–a 28% improvement compared to the 71% conversion obtained with the unmodified Pd/C catalyst. Furthermore, the selectivity increased from 88% (Pd/C, containing 7% *trans*-olefins and 5% over-hydrogenated byproducts) to 97% (Pd/C–NH_2, containing 2% *trans*-olefins and 1% over-hydrogenated byproducts) at full conversion. At a low conversion level (conversion < 30%, Fig. S27, and Table S6), the TOF of Pd/C–NH_2 reaches 3675 h^{-1}, which is 17-fold higher than that of the Lindlar catalyst (205 h^{-1}) and outperforms commercial Pd/C (2695 h^{-1}) and Pd/C (3094 h^{-1}). In comparison, the 0.1 wt% Pd/C–NH_2 catalyst achieved a mere 8% conversion for mifepristone, with a TOF of only 18 h^{-1}. Moreover, during the hydrogenation of phenylacetylene, Pd/C–NH_2 also demonstrates a performance advantage over some of the currently reported catalysts for phenylacetylene semi-hydrogenation (Table S7). AC-STEM imaging showed that the 0.1 wt% Pd/C–NH_2 catalyst contained mainly small Pd NPs along with a significant number of Pd SAs (Fig. S28 and S29). XPS analysis further revealed that 59% of the Pd species in the catalyst were present as Pd^{4+} (Fig. S30). This indicated that the sole Pd SAs exhibit intrinsic limitations in the hydrogenation reaction of mifepristone.

The time–course profile of Pd/C–NH_2 (Fig. 4d) showed that complete conversion of mifepristone was achieved within 30 min with 97% selectivity. In contrast, Pd/C required 60 min to reach full conversion with only 88% selectivity (Fig. 4e), demonstrating its inferior performance. When the reaction was extended to 180 min, Pd/C–NH_2 still retained 85% selectivity, whereas that of Pd/C decreased significantly to 66%, underscoring the good selectivity for Pd/C–NH_2. Therefore, the simultaneous enhancement in both activity and selectivity was achieved through the APTES-modified support, enabled by the

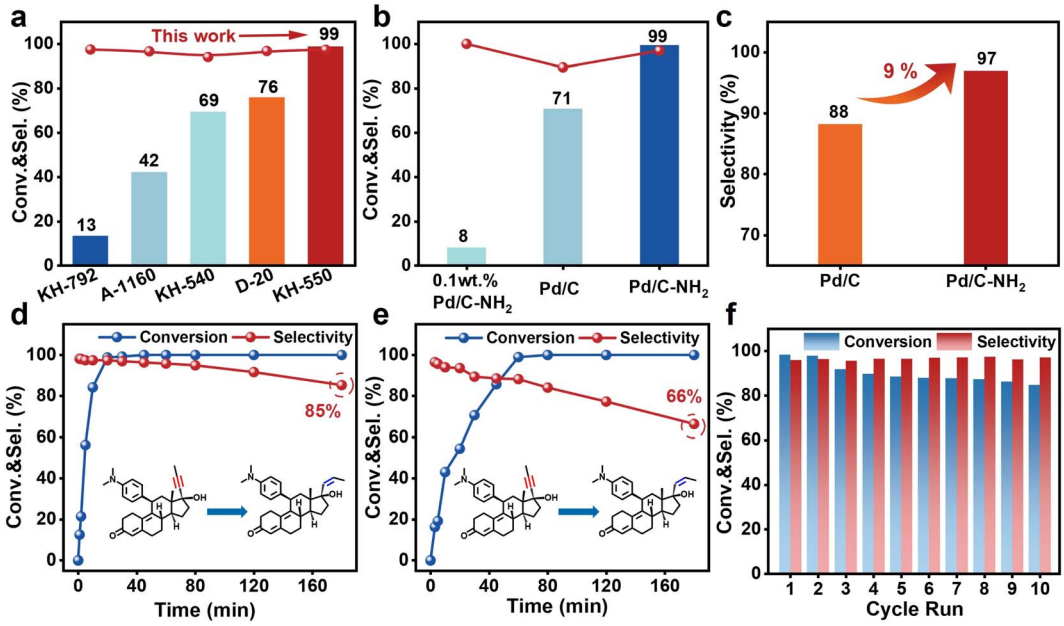

Fig. 4 Catalytic activity evaluation. (a) Comparison of catalytic performance of catalysts modified with different silane coupling agents. (b) Comparison of conversion of Pd/C–NH_2, Pd/C and 0.1 wt% Pd/C–NH_2. (c) Comparison of selectivity between Pd/C–NH_2 and Pd/C. (d and e) Time curves of Pd/C–NH_2 and Pd/C. (f) Stability cyclic test of Pd/C–NH_2. Reaction conditions: 250 mg mifepristone, 6 mg catalyst, 25 °C, 0.1 MPa.

coexistence of Pd_{IV} SA and Pd NP active sites. Beyond catalytic activity and selectivity, the stability of Pd/C–NH_2 and Pd/C was assessed through reuse over multiple reaction cycles (Fig. 4f, and S31). The Pd/C–NH_2 catalyst exhibited relatively stable performance over 10 consecutive reaction cycles, with activity declining from 99% to 85% while selectivity remained unchanged. This decrease in activity is likely attributable to valence state instability under H_2 reaction conditions. In contrast, Pd/C underwent more severe deactivation under identical cycling conditions, decreasing from 99% to 60%, which indicates that the stability of Pd/C–NH_2 is significantly superior to that of Pd/C. TEM observations showed that the particle size of Pd/C–NH_2 increased from 1.86 to 1.93 nm after recycling, with no significant aggregation detected, confirming the strong anchoring effect of –NH_2 ligands (Fig. S32–37). In contrast, Pd/C exhibited remarkable aggregation of Pd particles (>10 nm), which is the main cause of Pd/C deactivation. After recycling, Pd/C–NH_2 retained the characteristic infrared absorption peak of –NH_2 (Fig. S38), indicating that the ligands were firmly anchored and did not leach during the reaction. ICP-OES data showed that the Pd contents for the reused Pd/C–NH_2 and Pd/C are 4.71 wt% and 3.36 wt% (Table S1), respectively, which further demonstrating the strong anchoring effect of –NH_2 groups. XPS analysis of the recycled catalysts revealed that Pd^{4+} in Pd/C–NH_2 was partially reduced (Fig. S39), which would diminish the contribution of the Pd^{4+} mediated selective hydrogenation pathway and result in decreased catalytic activity.

Investigation on the action mechanism of Pd_{IV} SAs

To elucidate the specific role of Pd_{IV} SAs in Pd/C–NH_2 during the hydrogenation of mifepristone, reduction of the catalyst was conducted under relatively harsh conditions (60 °C, 0.5 MPa H_2, 4 h or 12 h in an autoclave) with the aim of reducing the Pd^{4+} species. AC-STEM images (Fig. 5a–c, S40 and S41) showed that even after reduction, the active Pd species in the catalyst still remained in the form of both SAs and NPs. XPS analysis revealed that the proportion of Pd^{4+} decreased from the original 30% to 13% and finally to 9% (Fig. S42), confirming the successful reduction of Pd^{4+}. When the reduced catalysts were applied to the hydrogenation of mifepristone (Fig. 5d, and S43), a significant decrease in catalytic activity was observed under identical conditions. After 12 h of reduction, the activity dropped to 65%. Furthermore, when the reaction time was extended to achieve full conversion of mifepristone, the selectivity decreased from 97% to 93%. To accurately quantify the

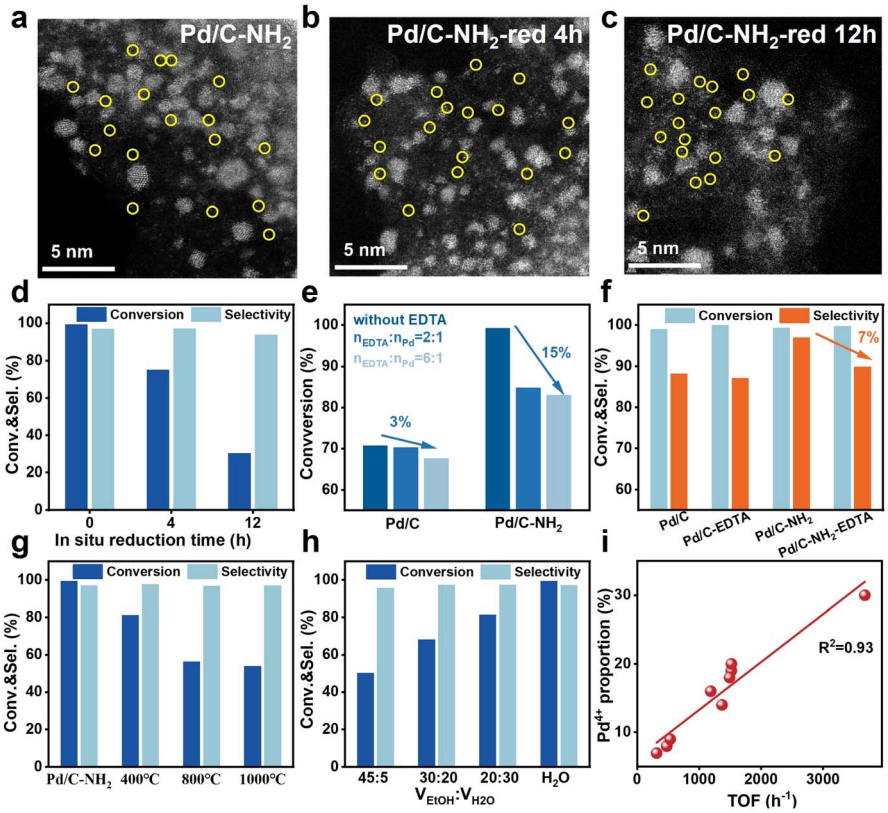

Fig. 5 Mechanism of Pd^{4+} on selective hydrogenation of mifepristone. (a–c) AC-STEM images of Pd/C–NH_2, Pd/C–NH_2-red 4 h and Pd/C–NH_2-red 12 h (reduction reaction conditions: 0.5 MPa, 60 °C). (d) Comparison of activity for Pd/C–NH_2, Pd/C–NH_2-red 4 h and Pd/C–NH_2-red 12 h catalysts under identical reaction conditions. (e) Comparison of activity between Pd/C and Pd/C–NH_2 poisoned with EDTA. (f) Comparison of selectivity for Pd/C and Pd/C–NH_2 under complete conversion conditions when $n_{EDTA} : n_{Pd} = 6 : 1$. (g) Comparison of catalytic performance with supports calculated at different calcination temperatures. (h) Comparison of catalytic performance with different $V_{EtOH} : V_{H_2O}$ catalysts for hydrolysis. (i) The linear fitting curve of TOF values *versus* Pd^{4+} content for different catalysts. Reaction conditions: 250 mg mifepristone, 6 mg catalyst, 25 °C, 0.1 MPa H_2, reaction for 30 min.

contribution of Pd_{IV} SA, we systematically adjusted the reaction conditions to compare the selectivity of all catalysts at similar conversion levels.[56] The experimental results indicate that, although 0.1 wt% Pd/C–NH_2 required a longer reaction time to achieve comparable conversion, its selectivity (100%, 98%, 98%) at conversion levels of 20%, 50%, and 80% was consistently higher than those of Pd/C–NH_2 (98%, 97%, 97%) and Pd/C (96%, 94%, 89%) (Fig. S44). This trend further confirms the crucial role of Pd_{IV} SAs in enhancing selectivity.

Ethylenediaminetetraacetic acid (EDTA) and potassium thiocyanate (KSCN) were used as selective poisoning agents to probe the respective contributions of Pd_{IV} SAs and Pd NPs to the reaction.[57,58] EDTA can selectively poison Pd SA sites, while KSCN can poison both Pd SA and Pd NP sites. As shown in Fig. 5e and S45, when $n_{EDTA} : n_{Pd} = 2 : 1$, the conversion of mifepristone over Pd/C–NH_2 decreased from 99% to 85%, while the selectivity remained largely unchanged. Increasing the ratio to $n_{EDTA} : n_{Pd} = 6 : 1$ led to a slight decrease in conversion to 83%. In contrast, for Pd/C, the same poison ratio resulted in only a 3% decrease in activity (from 71% to 68%). When the reaction time was extended to achieve full conversion (Fig. 5f), the selectivity of Pd/C remained almost unchanged, while that of Pd/C–NH_2 dropped from 97% to 90%. These results indicate that SAs are a key factor in enhancing the selectivity and activity in the selective hydrogenation of mifepristone and further confirm that Pd_{IV} SAs act as active sites. Poisoning experiments with KSCN showed that both Pd/C and Pd/C–NH_2 catalysts were completely deactivated at $n_{KSCN} : n_{Pd} = 2 : 1$, demonstrating that Pd is the sole active site in these catalysts. Subsequently, catalysts obtained through thermal treatment at different temperatures and those modified in different hydrolysis solvents also were also evaluated in the hydrogenation of mifepristone (Fig. 5g, and h). Catalytic activity gradually decreased with increasing thermal calcination temperature, but improved with a higher proportion of deionized water in the hydrolysis solvent. It is noteworthy that a significant linear correlation ($R^2 = 0.93$) was observed between the TOF values and the proportion of Pd^{4+} species (Fig. 5i and Table S8). This result indicates that the Pd^{4+} content not only modulates the reaction but also exhibits a positive correlation with the TOF, further confirming the critical role of Pd^{4+} species in the catalytic reaction from a kinetic perspective.

Mechanism analysis

To elucidate the superior activity of Pd/C–NH_2, the kinetic orders of H_2 and mifepristone were measured.[28,59,60] As shown in Fig. 6a, the reaction orders for H_2 on Pd/C and Pd/C–NH_2 are 1.41 and 0.59, respectively. The higher order on Pd/C suggests that H_2 dissociation likely requires multiple adjacent Pd sites, reflecting strong H_2 pressure dependence. In contrast, the reaction order of 0.59 for Pd/C–NH_2 implies that H_2 activation is not hindered by substrate competition. This is attributed to the facilitated dissociation of H_2 after –NH_2 modification, reducing its reliance on hydrogen concentration. As shown in Fig. 6b, the reaction orders for mifepristone on Pd/C and Pd/C–NH_2 are −0.37 and 0.12, respectively. The negative reaction order for Pd/C indicates strong adsorption of the reactant, which covers active sites and may even poison adjacent sites, leading to an overall decrease in activity. The nearly zero reaction order for Pd/C–NH_2 can be attributed to the presence of Pd_{IV} SAs. These SAs weaken the strong adsorption of mifepristone on Pd NPs, thereby alleviating the competitive adsorption between H_2 and mifepristone and enhancing hydrogen activation. To verify hydrogen spillover, tungsten oxide (WO_3) was physically mixed with the catalysts. The yellow WO_3 turns dark blue upon reaction with spilled hydrogen due to the formation of H_3WO_3.[61,62] After purging under flowing H_2 for 10 min, both Pd/C–WO_3 and Pd/C–NH_2–WO_3 changed from pale yellow to dark blue (Fig. S46). Notably, Pd/C–NH_2–WO_3 exhibited a more pronounced color change to deep green, indicating its stronger hydrogen spillover capability. Hydrogen temperature-programmed reduction (H_2-TPR) was subsequently performed to further investigate H_2 adsorption behavior. As shown in Fig. 6c, the low-temperature peaks correspond to the direct reduction of PdO_x,[63,64] while the high-temperature reduction peaks are attributed to support reduction induced by hydrogen spillover. Pd/C–NH_2 exhibits the largest peak area at 115 °C, and its support reduction temperature is significantly lowered from 539 °C (Pd/C) to 495 °C, indicating that –NH_2 modification enhances the low-temperature H_2 dissociation ability of Pd. For 0.1 wt% Pd/C–NH_2, the low-temperature reduction peak is relatively weak, suggesting limited H_2 dissociation capacity. Hydrogen spillover occurs at an early stage and the negative peak at 454 °C likely results from the reverse spillover and recombination release of previously spilled and stored hydrogen,[65] further confirming that –NH_2 modification promotes hydrogen spillover. Reactions conducted under H_2 and D_2 atmospheres, analyzed by both HPLC and ^1H NMR, consistently show that all three catalysts exhibit lower reaction rates under D_2 than under H_2, with Pd/C–NH_2 consistently demonstrating the highest activity (Fig. S47, S48 and Table S9). This indicates that Pd NPs are the key hydrogen source determining the overall reaction rate.[59] Approximately 9% of hydrogenated product (5.6 ppm) was detected in both Pd/C–NH_2 and Pd/C during deuteration reactions, confirming the participation of water in the reaction.[50] Notably, Pd/C–NH_2 yields a higher proportion of deuterated products, indirectly evidencing the occurrence of hydrogen spillover. Catalysts containing SAs exhibit higher hydrogen utilization efficiency and conversion rates within the same reaction time.[66,67] Although hydrogen spillover also occurs on Pd/C, the absence of suitable acceptors for the activated hydrogen renders the spilled hydrogen incapable of participating in hydrogenation. For 0.1 wt% Pd/C–NH_2, the scarcity of Pd NPs results in poor H_2 dissociation ability, making water the primary participant in the initial reaction stage and leading to inferior performance under equivalent conditions. Furthermore, after EDTA poisoning, the H_2 adsorption capacity (Table S2) of Pd/C–NH_2 decreases from 301.07 to 111.30 $\mu mol_{H_2}\ g_{Pd}^{-1}$, correlating with the observed decline in conversion. This confirms the role of Pd_{IV} SAs as critical hydrogen "acceptors".[52,66] When these sites are chelated by EDTA, spilled hydrogen cannot be effectively received and utilized, thereby disrupting the entire "activation–spillover–

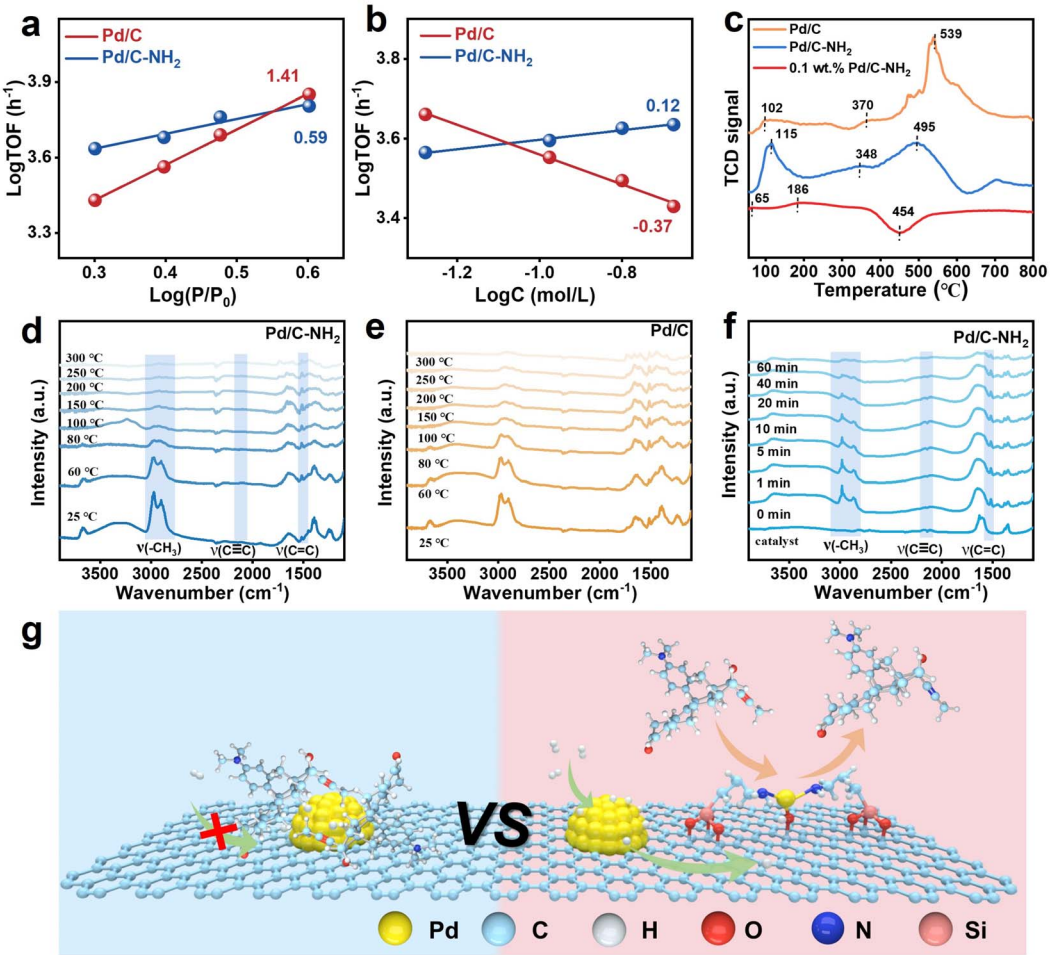

Fig. 6 Kinetic studies. (a and b) Kinetic orders with respect to (a) H_2 and (b) mifepristone over the Pd/C–NH_2 and Pd/C catalysts. (c) H_2-TPR of Pd/C, Pd/C–NH_2 and 0.1 wt% Pd/C–NH_2. (d and e) *In situ* FT-IR spectra showing the variation of adsorbed mifepristone on Pd/C–NH_2 and Pd/C with increasing temperature. (f) *In situ* FT-IR spectra showing the variation of adsorbed mifepristone on Pd/C–NH_2 with H_2 exposure time. (g) Reaction pathway on the Pd/C and Pd/C–NH_2 catalysts.

reaction" cycle. These findings further validate the hydrogen spillover mechanism from Pd NPs to Pd SAs. H_2 dissociation occurs on Pd NPs, and efficient migration and exchange of active hydrogen (effective hydrogen spillover) can only be achieved when both Pd NPs and SAs coexist.

Subsequently, the catalyst was exposed to a certain amount of mifepristone/THF solution, and its desorption behavior was observed under temperature ramping with N_2 purging. From the spectroscopic data, the characteristic functional groups of mifepristone –CH_3, C≡C, and C=C are located at 2980, 2862, 2088, and 1520 cm^{-1},[60,68–70] respectively. Mifepristone desorbed completely from Pd/C–NH_2 at 200 °C, while on Pd/C, the temperature had to rise to 250 °C or even higher (Fig. 6d, e and S49). On 0.1 wt% Pd/C–NH_2, desorption occurred at 100 °C, indicating stronger adsorption of mifepristone on Pd/C. Substrate adsorption experiments were conducted to verify this conclusion, and the corresponding XPS results are shown in Fig. S50. The change in binding energy after mifepristone adsorption on Pd/C–NH_2 (+0.2 eV) was smaller than that on Pd/C (+0.38 eV), indicating a weaker electronic interaction between Pd/C–NH_2 and mifepristone.[28] The introduction of SAs weakened the strong adsorption of mifepristone on NPs, thereby providing more active sites for hydrogen dissociation and enhancing catalytic activity. Furthermore, *in situ* infrared spectroscopy was used to monitor changes in mifepristone adsorbed on the catalyst during 25 °C hydrogenation. It was found that on Pd/C–NH_2, the characteristic peaks of mifepristone weakened and eventually disappeared within 60 min after introducing H_2. The fundamental reason is that the triple bond in the alkyne side chain was hydrogenated to a double bond, and the propargyl methyl group attached to an sp-hybridized carbon transformed into a common sp^2-hybridized allyl methyl group, leading to a decrease in the C–H bond vibration frequency. No distinct product peaks were observed because the key new characteristic peaks of the product, aglepristone, overlapped with strong substrate peaks. On Pd/C, this process required 90 min, while on 0.1 wt% Pd/C–NH_2, the peaks remained largely unchanged even after 120 min (Fig. 6f, and S49), further demonstrating the superior performance of Pd/C–NH_2.

Based on the above experiments and characterization studies, a reaction mechanism for mifepristone hydrogenation on the catalysts is proposed (Fig. 6g). On Pd/C, H_2 and the substrate compete for adsorption on Pd NP surfaces. The strong substrate adsorption lowers H_2 activation efficiency, inhibiting hydrogenation activity and promoting over-hydrogenation. In contrast, Pd/C–NH_2, which contains both Pd_{IV} SA and Pd NP active sites, enables an alternative hydrogenation pathway. Here, H_2 is dissociated and activated on Pd NPs, followed by hydrogen spillover to Pd_{IV} SAs, where it reacts with mifepristone adsorbed on the SAs. In this pathway, the weaker adsorption of mifepristone on Pd_{IV} SAs allows the semi-hydrogenated product to desorb readily without over-hydrogenation. This dual-site mechanism[38,52] contributes to simultaneous enhancement of both activity and selectivity.

Conclusions

In summary, this study demonstrates a ligand modification strategy for the controlled synthesis of synergistic catalytic centers coexisting Pd_{IV} SAs and Pd NPs, enabling highly efficient and selective hydrogenation of mifepristone. A "grafting-then-coordination" approach facilitated Pd–N/O coordination assisted by both oxygen-containing functional groups and amine ligands on the support surface, leading to the stabilization of Pd_{IV} SAs. Under mild conditions, the Pd/C–NH_2 catalyst exhibited outstanding catalytic performance, achieving 99% conversion and 97% selectivity in the selective hydrogenation of mifepristone, significantly surpassing Pd/C. The electron-deficient nature of Pd_{IV} SAs mitigates substrate poisoning on Pd NP sites, thereby enhancing H_2 activation. Concurrently, H_2 activated on Pd NPs undergoes spillover to the hydrogen-deficient Pd_{IV} SAs, promoting hydrogenation of mifepristone adsorbed on the Pd_{IV} SA sites. The present ligand modification strategy enables the formation of Pd_{IV} SAs that transform conventional poisoning sites into productive active centers. The collaborative effect between Pd_{IV} SAs and Pd NPs provides a novel pathway for the selective hydrogenation of mifepristone and offers valuable insights for the rational design of catalysts for steroidal drug synthesis.

Author contributions

M. J. major experimental production, formal analysis, methodology, investigation, data curation, writing – original draft. Y. L. experimental production, methodology, visualization. X. L., Z. X. Y., C. M. C. and Y. M. H. validation, formal analysis, data curation, writing – review & editing. F. J. S., X. N. L., J. X. H. and S. D. visualization, writing – review & editing. Z. Z. W: methodology, conceptualization, resources, supervision, project administration, writing – review & editing. J. G. W: methodology, funding acquisition, resources, supervision, project administration, writing – review & editing.

Conflicts of interest

The authors declare no competing financial interests.

Data availability

The authors confirm that the data supporting the findings of this study are available within the article and its supplementary information (SI). The data supporting this article have been included as part of the supporting information. Supplementary information: chemicals, catalyst evaluation and analysis and catalyst characterization. Characterization data, NMR spectra, HPLC traces, and additional figures supporting the results presented in the main text. See DOI: https://doi.org/10.1039/d5sc08632a.

Acknowledgements

The authors acknowledge the financial support from the National Natural Science Foundation of China (22378354, 22008213, 22494711, and U21A20298), the Zhejiang Provincial Natural Science Foundation (LR26B060002, LQ21B060005), and the Fundamental Research Funds for the Provincial Universities of Zhejiang (RFA2022011).

References

1 V. Gianvito, A.-B. Neyvis, M. Sharon, L. Núria and P.-R. Javier, From the Lindlar catalyst to supported ligand-modified palladium nanoparticles: selectivity patterns and accessibility constraints in the continuous-flow three-phase hydrogenation of acetylenic compounds, *Chem*, 2014, **20**(20), 5926–5937.

2 S. Run, W. Zeping, Z. Yunxuan, G. I. N. Waterhouse, L. Zhenhua, Z. Bikun, S. Zhimei, X. Chuan, W. Haotian and Z. Tierui, Room-temperature electrochemical acetylene reduction to ethylene with high conversion and selectivity, *Nat. Catal.*, 2021, **4**(7), 565–574.

3 F. Xianbiao, L. Jian, K. Siriluk, H. Xiaobing, Y. Qin, T. D. G, H. J. T and K. Yijin, Two-Dimensional Pd Rafts Confined in Copper Nanosheets for Selective Semihydrogenation of Acetylene, *Nano Lett.*, 2021, **21**(13), 5620–5626.

4 C. Xiao, S. Chuang and L. Changhai, Highly selective catalysts for the hydrogenation of alkynols: A review, *Chin. J. Catal.*, 2021, **42**(12), 2105–2121.

5 T. Yuping, L. Nianguang, D. Jin-ao and T. Weiwei, Structure, bioactivity, and chemical synthesis of OSW-1 and other steroidal glycosides in the genus Ornithogalum, *Chem. Rev.*, 2013, **113**(7), 5480–5514.

6 C. A. Sanhueza, M. M. Baksh, B. Thuma, M. D. Roy, S. Dutta, C. Préville, B. A. Chrunyk, K. Beaumont, R. Dullea, M. Ammirati, S. Liu, D. Gebhard, J. E. Finely, C. Salatto, A. King-Ahmad, I. Stock, K. Atkinson, B. Reidich, W. Lin, R. Kumar, M. Tu, E. Menhaji-Klotz, D. Price, S. Liras, M. Finn and V. Mascitti, Efficient Liver Targeting by Polyvalent Display of a Compact Ligand for the Asialoglycoprotein Receptor, *J. Am. Chem. Soc.*, 2017, **139**(9), 3528–3536.

7 J. García-Calvo, P. Calvo-Gredilla, S. Vallejos, J. M. García, J. V. Cuevas-Vicario, G. García-Herbosa, M. Avella and T. Torroba, Palladium nanodendrites uniformly deposited

on the surface of polymers as an efficient and recyclable catalyst for direct drug modification via Z-selective semihydrogenation of alkynes, *Green Chem.*, 2018, **20**(16), 3875–3883.

8 C. A. Sanhueza, M. M. Baksh, B. Thuma, M. D. Roy, S. Dutta, C. Préville, B. A. Chrunyk, K. Beaumont, R. Dullea, M. Ammirati, S. Liu, D. Gebhard, J. E. Finley, C. T. Salatto, A. King-Ahmad, I. Stock, K. Atkinson, B. Reidich, W. Lin, R. Kumar, M. Tu, E. Menhaji-Klotz, D. A. Price, S. Liras, M. G. Finn and V. Mascitti, Efficient Liver Targeting by Polyvalent Display of a Compact Ligand for the Asialoglycoprotein Receptor, *J. Am. Chem. Soc.*, 2017, **139**(9), 3528–3536.

9 R. Bai, G. He, L. Li, T. Zhang, J. Li, X. Wang, X. Wang, Y. Zou, D. Mei, A. Corma and J. Yu, Encapsulation of Palladium Carbide Subnanometric Species in Zeolite Boocsts Highly Selective Semihydrogenation of Alkynes, *Angew. Chem., Int. Ed.*, 2023, **62**(48), e202313101.

10 Z. Wei, X. Liu, M. Wang, Y. Lv, S. Huang, J. Wang, M. Jiang, Z. Yang, Z. Yao, S. Dai, X. Li and J. Wang, Reaction-driven self-adapting Pd/Nb_2O_5 steering alkyne semi-hydrogenation, *Cell Rep. Phys. Sci.*, 2025, **6**(8), 102770.

11 J. Xiong, S. Mao, Q. Luo, H. Ning, B. Lu, Y. Liu and Y. Wang, Mediating trade-off between activity and selectivity in alkynes semi-hydrogenation via a hydrophilic polar layer, *Nat. Commun.*, 2024, **15**(1), 1228.

12 Y. Geng, X. Guo, F. Yue, M. Xiang and Q. Zhu, Mass Production of Multishell Hollow SiO_2 Spheres With Adjustable Void Ratios and Pore Structures, *Adv. Mater.*, 2024, **36**(45), e2409421.

13 Z. A. Qiao, P. Zhang, S. H. Chai, M. Chi, G. M. Veith, N. C. Gallego, M. Kidder and S. Dai, Lab-in-a-shell: encapsulating metal clusters for size sieving catalysis, *J. Am. Chem. Soc.*, 2014, **136**(32), 11260–11263.

14 S. Wang, Y. Wang, X. Wu, C. Hu, H. Zhang, Q. Cui, X. Bao and P. Yuan, Pore-size dependent catalytic activity of supported Pd catalysts for selective hydrogenation of nitrile butadiene rubber, *Chem. Eng. Sci.*, 2023, **273**, 118629.

15 X. Ge, Y. Jing, W. Wang, Y. Cao, J. Zhang, G. Qian, H. Jiang, X. Zhou, D. Chen, W. Yuan and X. Duan, Synergizing Pd_1Sb_2 Site with Neighboring Near-Surface Pd Site to Break the Trade-Off between Selectivity and Activity of Alkyne Semihydrogenation, *J. Am. Chem. Soc.*, 2025, **147**(33), 30178–30189.

16 D. Teschner, J. Borsodi, A. Wootsch, Z. Révay, M. Hävecker, A. Knop-Gericke, S. D. Jackson and R. Schlögl, The Roles of Subsurface Carbon and Hydrogen in Palladium-Catalyzed Alkyne Hydrogenation, *Science*, 2008, **320**(5872), 86–89.

17 N. Cherkasov, D. Y. Murzin, C. R. A. Catlow and A. Chutia, Selectivity of the Lindlar catalyst in alkyne semi-hydrogenation: a direct liquid-phase adsorption study, *Catal. Sci. Technol.*, 2021, **11**(18), 6205–6216.

18 C. N. Filer, Terminal alkyne semi-tritiation with Lindlar catalyst and its mechanism implications, *J. Radioanal. Nucl. Chem.*, 2020, **326**(3), 1727–1732.

19 U. P. Laverdura, L. Rossi, F. Ferella, C. Courson, A. Zarli, R. Alhajyoussef and K. Gallucci, Selective Catalytic Hydrogenation of Vegetable Oils on Lindlar Catalyst, *ACS Omega*, 2020, **5**(36), 22901–22913.

20 Z. Zhao, L. Gao, X. An, W. Zhang, X. Ren, J. Wang, J. Yan and H. Zhang, Electronic metal-support interaction engineering in MXene-derived Cu-ZnO/Nb2C@Nb2O5 for efficient CO2 hydrogenation to methanol, *Appl. Catal., B*, 2026, **382**, 126000.

21 M. Jorgensen and H. Gronbeck, Selective Acetylene Hydrogenation over Single-Atom Alloy Nanoparticles by Kinetic Monte Carlo, *J. Am. Chem. Soc.*, 2019, **141**(21), 8541–8549.

22 J. Liu, M. B. Uhlman, M. M. Montemore, A. Trimpalis, G. Giannakakis, J. Shan, S. Cao, R. T. Hannagan, E. C. H. Sykes and M. Flytzani-Stephanopoulos, Integrated Catalysis-Surface Science-Theory Approach to Understand Selectivity in the Hydrogenation of 1-Hexyne to 1-Hexene on PdAu Single-Atom Alloy Catalysts, *ACS Catal.*, 2019, **9**(9), 8757–8765.

23 R. Gao, J. Xu, J. Wang, J. Lim, C. Peng, L. Pan, X. Zhang, H. Yang and J.-J. Zou, Pd/Fe_2O_3 with Electronic Coupling Single-Site Pd–Fe Pair Sites for Low-Temperature Semihydrogenation of Alkynes, *J. Am. Chem. Soc.*, 2021, **144**(1), 573–581.

24 L. Qiao, X. Wang, S. Zong, Z. Huang, Z. Zhou, M. Fan and Y. Yao, Anion-Doping-Mediated Metal–Support Interactions in CeO_2-Supported Pd Catalysts for CO_2 Hydrogenation, *ACS Catal.*, 2024, **14**(17), 13181–13194.

25 X. Song, F. Shao, Z. Zhao, X. Li, Z. Wei and J. Wang, Single-Atom Ni-Modified Al2O3-Supported Pd for Mild-Temperature Semi-hydrogenation of Alkynes, *ACS Catal.*, 2022, **12**(24), 14846–14855.

26 B. Li, W. He, J. Liu, X. Zhang, R. Fang, X. Zhang, Z. Shi, C. Lu, F. Feng, Q. Zhang, Q. Wang and X. Li, In Situ Sulfide-Induced Surface Reconstruction of Catalysts for Enhanced Hydrogenation Efficiency and Sulfur Resistance, *ACS Catal.*, 2025, **15**(10), 7810–7822.

27 Q. Li, S. Liu, J.-C. Liu, Z. Li and Y. Li, Recycling Sulfur-Poisoned Pd Catalysts via Thermal Atomization for Semi-Hydrogenation of Acetylene, *J. Am. Chem. Soc.*, 2024, **147**(7), 5615–5623.

28 Z. Wei, G. Dong, L. Zhao, S. Huang, M. Xia, W. Huang, M. Jiang, Z. Yang, Z. Yao, J. Li and J. Wang, Enhanced resistance to poisoning of Pd in alkynes semi-hydrogenation by metal-ligand electronic interactions, *AIChE J.*, 2024, **71**(3), e18687.

29 J. Zhang, W. Wang, J. Chen, X. Cai, L. Yang, M. Peng, Y. Wang, Y. Si, F. Hong, X. Chen, B. Sun, J. Diao, L. Jin, G. Wang, D. Ma and H. Liu, Amino Nests Boost Pd/SiO_2 Single-Atom Catalysts for Efficient Selective Semi-Hydrogenation of Acetylene, *Angew. Chem., Int. Ed.*, 2025, e202515937.

30 L. Kunlong, Q. Ruixuan and Z. Nanfeng, Insights into the Interfacial Effects in Heterogeneous Metal Nanocatalysts toward Selective Hydrogenation, *J. Am. Chem. Soc.*, 2021, **143**(12), 4483–4499.

31 J. Zhang, Y. Deng, X. Cai, Y. Chen, M. Peng, Z. Jia, Z. Jiang, P. Ren, S. Yao, J. Xie, D. Xiao, X. Wen, N. Wang, H. Liu

and D. Ma, Tin-Assisted Fully Exposed Platinum Clusters Stabilized on Defect-Rich Graphene for Dehydrogenation Reaction, *ACS Catal.*, 2019, **9**(7), 5998–6005.

32 Q. Botao, W. Aiqin, Y. Xiaofeng, A. L. F, J. Zheng, C. Yitao, L. Jingyue, L. Jun and Z. Tao, Single-atom catalysis of CO oxidation using Pt_1/FeOx, *Nat. Chem.*, 2011, **3**(8), 634–641.

33 W. Ligang, W. Jiabin, W. Shunwu, L. Huan, W. Yao and W. Dingsheng, The reformation of catalyst: From a trial-and-error synthesis to rational design, *Nano Res.*, 2023, **17**(4), 3261–3301.

34 Z. Xiaobo, L. Beibei, W. Qishun, W. Dingsheng and L. Yadong, Emerging low-nuclearity supported metal catalysts with atomic level precision for efficient heterogeneous catalysis, *Nano Res.*, 2022, **15**(9), 7806–7839.

35 R. Bai, G. He, J. Li, L. Li, T. Zhang, X. Wang, W. Zhang, Y. Zou, J. Zhang, D. Mei, A. Corma and J. Yu, Heteroatoms-Stabilized Single Palladium Atoms on Amorphous Zeolites: Breaking the Tradeoff between Catalytic Activity and Selectivity for Alkyne Semihydrogenation, *Angew. Chem., Int. Ed.*, 2024, **63**(44), e202410017.

36 W. Gong and L. Kang, BNPd single-atom catalysts for selective hydrogenation of acetylene to ethylene: a density functional theory study, *R. Soc. Open Sci.*, 2018, **5**(7), 171598.

37 Y. Liu, B. Wang, Q. Fu, W. Liu, Y. Wang, L. Gu, D. Wang and Y. Li, Polyoxometalate-Based Metal-Organic Framework as Molecular Sieve for Highly Selective Semi-Hydrogenation of Acetylene on Isolated Single Pd Atom Sites, *Angew. Chem., Int. Ed.*, 2021, **60**(41), 22522–22528.

38 Z. Chen, C. Wang, B. Zhang, J. Li, D. Wang, G. Xu, J. Zhang, M. Peng, D. Ma and Y. Zhang, Interface Modification of Single Atom-Nanocluster Synergistic Sites to Break the Activity-Selectivity-Stability Trade-Off in Selective Hydrogenations, *Adv. Mater.*, 2025, **37**(32), e2503841.

39 J. Bruns, D. van Gerven, T. Kluner and M. S. Wickleder, Palladium(IV) in an Oxoanionic Environment: The XeF_2 Assisted Synthesis of $[Pd(S_2O_7)_3]_2$, *Angew. Chem., Int. Ed.*, 2016, **55**(28), 8121–8124.

40 V. Goudy, A. Jaoul, M. Cordier, C. Clavaguera and G. Nocton, Tuning the Stability of Pd(IV) Intermediates Using a Redox Non-innocent Ligand Combined with an Organolanthanide Fragment, *J. Am. Chem. Soc.*, 2017, **139**(31), 10633–10636.

41 Y. Zhang, Y. Cheng, X. Wang, Q. Sun, X. He and H. Ji, Enhanced Hydrogenation Properties of Pd Single Atom Catalysts with Atomically Dispersed Ba Sites as Electronic Promoters, *ACS Catal.*, 2022, **12**(24), 15091–15096.

42 R. Gao, J. Xu, J. Wang, J. Lim, C. Peng, L. Pan, X. Zhang, H. Yang and J.-J. Zou, Pd/Fe_2O_3 with Electronic Coupling Single-Site Pd–Fe Pair Sites for Low-Temperature Semihydrogenation of Alkynes, *J. Am. Chem. Soc.*, 2022, **144**(1), 573–581.

43 F. Zhang, H. Jiang, X. Li, X. Wu and H. Li, Amine-Functionalized GO as an Active and Reusable Acid–Base Bifunctional Catalyst for One-Pot Cascade Reactions, *ACS Catal.*, 2013, **4**(2), 394–401.

44 C. Mao, Z. Chen, J. Zhang, Z. Tang, H. Jiang and R. Chen, Synergistic Effects of Hierarchically Porous Structures and Amino Groups in Pd@MOFs for the Selective Hydrogenation of Phenol, *Ind. Eng. Chem. Res.*, 2023, **62**(34), 13440–13449.

45 H. Liu, Y. Zhang, L. Zhang, X. Mu, L. Zhang, S. Zhu, K. Wang, B. Yu, Y. Jiang, J. Zhou and F. Yang, Unveiling Atomic-Scaled Local Chemical Order of High-Entropy Intermetallic Catalyst for Alkyl-Substitution-Dependent Alkyne Semihydrogenation, *J. Am. Chem. Soc.*, 2024, **146**(29), 20193–20204.

46 J. Li, J. Kou, Y. Xiang, M. Chen, J. Zhang, X. Zhan, H. Zhang, F. Wang and Z. Dong, ZIF-8 derived N-doped porous carbon confined ultrafine PdNi bimetallic nanoparticles for semi-hydrogenation of alkynes, *Mol. Catal.*, 2023, **535**, 112865.

47 R. Zhang, Z. Liu, S. Zheng, L. Wang, L. Zhang and Z. A. Qiao, Pyridinic Nitrogen Sites Dominated Coordinative Engineering of Subnanometric Pd Clusters for Efficient Alkynes' Semihydrogenation, *Adv. Mater.*, 2023, **35**(11), 2209635.

48 H. Pan, Y. Peng, X. Lu, J. He, L. He, C. Wang, F. Yue, H. Zhang, D. Zhou and Q. Xia, Well-constructed Ni@CN material derived from di-ligands Ni-MOF to catalyze mild hydrogenation of nitroarenes, *Mol. Catal.*, 2020, **485**, 110838.

49 Y. Li, Y. Xu, S. Chen, X. Shi, Q. Gu, L. Wang, M. Gu, B. Teng, B. Yang and J. Lu, Tuning the Electronic Structures of Anchor Sites to Achieve Zero-Valence Single-Atom Catalysts for Advanced Hydrogenation, *Angew. Chem., Int. Ed.*, 2024, **63**(35), e202406262.

50 E. Zhao, W. Kong, G. Zoppellaro, Y. Yang, B. Nan, L. Li, W. Zhang, Z. Chen, A. Bakandritsos, Z. J. Wang, M. Beller, R. Zboril and Z. Chen, Atomic Scale Engineering of Multivalence-State Palladium Photocatalyst for Transfer Hydrogenation with Water as a Proton Source, *Adv. Mater.*, 2025, **37**(32), e2504108.

51 J. Tian, R. Kong, Z. Wang, L. Fang, T. He, D. Jiang, H. Peng, T. Sun, Y. Zhu and Y. Wang, Enhancing Methane Combustion Activity by Modulating the Local Environment of Pd Single Atoms in Pd_1/CeO_2 Catalysts, *ACS Catal.*, 2024, **14**(1), 183–191.

52 S. Wang, Z. Guo, L. Wang, Y. Zeng, X. Liang, F. Dong, P. Zhu, H. Liu, D. Wang and Y. Li, Atomically Dispersed Palladium Catalyst for Chemoselective Hydrogenation of Quinolines, *Nano Lett.*, 2024, **24**(40), 12666–12675.

53 K. Fu and L. Shi, Enabling Site-Selective C-H Functionalization of Aliphatic Alcohols and Amines with exo-Directing Groups by Tether-Tunable Design of Pd_{II}/Pd_{IV} Catalysis, *ACS Catal.*, 2024, **14**(22), 17077–17083.

54 R. Wang, Y. Zheng, L. Hou, W.-C. Li and A.-H. Lu, Density regulation of surface hydroxyl on porous carbons as efficient catalytic supports, *Carbon*, 2025, **242**, 120469.

55 G. A. Castillo, L. Wilson, K. Efimenko, M. D. Dickey, C. B. Gorman and J. Genzer, Amidation of Polyesters Is Slow in Nonaqueous Solvents: Efficient Amidation of Poly(ethylene terephthalate) with 3-Aminopropyltriethoxysilane in Water for Generating Multifunctional Surfaces, *ACS Appl. Mater. Interfaces*, 2016, **8**(51), 35641–35649.

56 J. Audevard, J. Navarro-Ruiz, V. Bernardin, Y. Tison, A. Corrias, I. Del Rosal, A. Favre-Réguillon, R. Philippe,

I. C. Gerber and P. Serp, Adjustment of the Single Atom/Nanoparticle Ratio in Pd/CNT Catalysts for Phenylacetylene Selective Hydrogenation, *ChemCatChem*, 2023, **15**(11), e202300036.

57 W. Liu, L. Zhang, X. Liu, X. Liu, X. Yang, S. Miao, W. Wang, A. Wang and T. Zhang, Discriminating Catalytically Active FeN(x) Species of Atomically Dispersed Fe-N-C Catalyst for Selective Oxidation of the C-H Bond, *J. Am. Chem. Soc.*, 2017, **139**(31), 10790–10798.

58 B. Lu, L. Guo, F. Wu, Y. Peng, J. E. Lu, T. J. Smart, N. Wang, Y. Z. Finfrock, D. Morris, P. Zhang, N. Li, P. Gao, Y. Ping and S. Chen, Ruthenium atomically dispersed in carbon outperforms platinum toward hydrogen evolution in alkaline media, *Nat. Commun.*, 2019, **10**(1), 631.

59 Q. Luo, H. Wang, Q. Xiang, Y. Lv, J. Yang, L. Song, X. Cao, L. Wang and F. S. Xiao, Polymer-Supported Pd Nanoparticles for Solvent-Free Hydrogenation, *J. Am. Chem. Soc.*, 2024, **146**(38), 26379–26386.

60 Z. Wei, S. Huang, J. Li, Y. Lv, Z. Yao, G. Dong, M. Xia, Z. Yang, M. Jiang, S. Dai and J. Wang, Reaction sites optimization mediated by ligand coverage for semi-hydrogenation of different alkynes, *AIChE J.*, 2025, **71**(7), e18752.

61 M. Tan, Y. Yang, Y. Yang, J. Chen, Z. Zhang, G. Fu, J. Lin, S. Wan, S. Wang and Y. Wang, Hydrogen spillover assisted by oxygenate molecules over nonreducible oxides, *Nat. Commun.*, 2022, **13**(1), 1457.

62 R. P. Zhang, B. He, X. Liu and A. H. Lu, Hydrogen Spillover-Driven Dynamic Evolution and Migration of Iron Oxide for Structure Regulation of Versatile Magnetic Nanocatalysts, *J. Am. Chem. Soc.*, 2023, **145**(47), 25834–25841.

63 H. Wang, T. Xie, Y. Zhang, Y. Wang, C. Huang, L. Zheng, C. Ma and S. Sun, Ultra-low palladium single-atom catalysts enabled by strong metal support interactions for high-efficiency methanol steam reforming, *Chem. Eng. J.*, 2025, **523**, 168711.

64 K. Tian, S. Chen, G. Sun, J. Sun, X. Wang, J. Cai, Z. Wang, D. Fu, Z.-J. Zhao, C. Pei and J. Gong, Unraveling the hydrogen spillover in tandem propane dehydrogenation and reverse water gas shift reaction, *Nat. Commun.*, 2025, **16**(1), 10186.

65 J. Chen, S. Xiong, H. Liu, J. Shi, J. Mi, H. Liu, Z. Gong, L. Oliviero, F. Mauge and J. Li, Reverse oxygen spillover triggered by CO adsorption on Sn-doped Pt/TiO_2 for low-temperature CO oxidation, *Nat. Commun.*, 2023, **14**(1), 3477.

66 Y. Ma, Y. Ren, Y. Zhou, W. Liu, W. Baaziz, O. Ersen, C. Pham-Huu, M. Greiner, W. Chu, A. Wang, T. Zhang and Y. Liu, High-Density and Thermally Stable Palladium Single-Atom Catalysts for Chemoselective Hydrogenations, *Angew. Chem., Int. Ed.*, 2020, **59**(48), 21613–21619.

67 Y. Kim and D. H. Kim, Support-Dependent Formic Acid Dehydrogenation over Pd-Supported Catalysts Induced by Hydrogen Spillover, *Energy Fuels*, 2025, **39**(34), 16399–16406.

68 X. Ma, Z. An, H. Song, X. Shu, X. Xiang and J. He, Atomic Pt-Catalyzed Heterogeneous Anti-Markovnikov C-N Formation: Pt_1^0 Activating N-H for $Pt_1^{\delta+}$-Activated C = C Attack, *J. Am. Chem. Soc.*, 2020, **142**(19), 9017–9027.

69 K. D. Doney, D. Zhao and H. Linnartz, High-Resolution Infrared Spectra of the nu(1) Fundamental Bands of Mono-Substituted ^{13}C Propyne Isotopologues, *J. Phys. Chem. A*, 2018, **122**(2), 582–589.

70 Y. Zhao, J. Xu, K. Huang, W. Ge, Z. Liu, C. Lian, H. Liu, H. Jiang and C. Li, Dopant-and Surfactant-Tuned Electrode-Electrolyte Interface Enabling Efficient Alkynol Semi-Hydrogenation, *J. Am. Chem. Soc.*, 2023, **145**(11), 6516–6525.